Ionic shortcut currents via manifolds in reverse electrodialysis stacks

A. Culcasi, L. Gurreri, A. Zaffora, A. Cosenza, A. Tamburini[*], A. Cipollina, G. Micale

Dipartimento di Ingegneria, Università degli Studi di Palermo, Viale delle Scienze ed. 6, 90128 Palermo, Italy

ABSTRACT

Reverse electrodialysis (RED) is a blue energy technology for clean and sustainable electricity harvesting from the mixing entropy of salinity gradients. Recently, many efforts have been devoted to improving the performance of RED units by developing new ion-exchange membranes and by reducing the detrimental phenomena affecting the process. Among these sources of "irreversibility", the shortcut currents (or parasitic currents) flowing through alternative pathways may affect the process efficiency. Although such phenomena occur in several electrochemical processes (e.g. fuel cells, bipolar plate cells and vanadium redox flow batteries), they have received a poor attention in RED units. In this work, a process simulator with distributed parameters was developed and experimentally validated to characterize the shortcut currents and to assess their impact in RED stack performance under different designs and operating conditions. Results showed that shortcut currents can play a crucial role in stacks with a large number of cell pairs when the electrical resistance of the parasitic pathways is relatively low, e.g. configurations with concentrated brines, high resistance membranes, short channels or large manifolds. Future designs of efficient industrial-scale units cannot ignore these aspects. Finally, the model can be easily adapted for the simulation of electrodialysis and other electromembrane processes.

1. Introduction

1.1. Background

The production of sustainable energy is one of the main technological challenges of our time. Using renewable energy sources is a possible way to face the task. Among them, Salinity Gradient Energy (SGE, or blue energy or osmotic energy) can be harvested through proper-engineered systems exploiting the Gibbs free energy of mixing of two solutions at different salt concentrations [64]. Reverse Electrodialysis (RED) [2] is among the most investigated SGE technologies [3].

The RED process is carried out in a stack (Fig. 1) equivalent to a conventional electrodialysis (ED) unit, composed of several repetitive units, called "cell pairs", sandwiched between two end-plates containing the electrode compartments. Each cell pair consists of a Cation-Exchange Membrane (CEM), an Anion-Exchange Membrane (AEM), a concentrate channel and a diluate channel. In RED, the co-ion exclusion (or Donnan exclusion) gives rise to an electric potential over each membrane to equilibrate the chemical potential difference between the two solutions [4,5]. The sum of all the membrane potentials is, ideally, the open circuit voltage (OCV) of the stack. When the circuit is closed, redox reactions (typically occurring with a reversible couple) take place [6], converting the internal ions current (selective transport from concentrate to diluate) into an external electrons current. Thus, electric energy is supplied to an external load, which is the final user.

Net spacers or membrane profiles create the channels for the passage of the electrolyte solutions in ED/RED units. Spacers can also act against concentration polarization, yet increasing the Ohmic resistance and the pressure drops [7,8]. Holes in spacers gaskets and in membranes act as manifolds for distributing/collecting the two solutions to/from the compartments in separate hydraulic circuits.

Pattle carried out a pioneering work on RED in 1954, attaining a power density of 0.2 W/m^2 [9]. Since then, significant improvements have been achieved, especially in the last decade. With artificial seawater and river water at ambient temperature, Vermaas et al. [10] reported gross power densities up to 2.2 W/m^2, while Kim et al. [11] reached slightly higher values (2.4 W/m^2) by developing high-performing IEMs. Higher values can be attained by increasing the driving force in stacks fed in the concentrate by brines [12], which can be drawn from industrial processes (e.g. desalination), hypersaline lakes and saltworks [13–16]. A power output up to 1.35 W m^{-2} was reached by a full-scale RED pilot plant [17]. The highest power density, reported by Daniilidis et al. [18], was of 6.7 W m^{-2} (5 M - 0.01 M NaCl solutions at 60 °C). Net power is a very important performance indicator, given by the produced gross power minus the power spent for pumping the solutions. The maximization of net power density has been often used

Nomenclature

Acronyms

AEM	Anion-Exchange Membrane
CEM	Cation-Exchange Membrane
CFD	Computational Fluid Dynamics
DSA	Dimensionally Stable Anodes
ED	ElectroDialysis
IEM	Ion-Exchange Membrane
OCV	Open Circuit Voltage
RED	Reverse ElectroDialysis
SGE	Salinity Gradient Energy

Latin letters

A_Λ (-)	first Jones and Dole solution conductivity salt parameter
b (m)	spacer width
B_Λ (-)	second Jones and Dole solution conductivity salt parameter
C (mol m^{-3})	salt concentration in the solution
C_Λ (-)	third Jones and Dole solution conductivity salt parameter
d (m)	generic thickness
D (m^2 s^{-1})	salt diffusivity
EMF (V)	cell pair electromotive force
F (C mol^{-1})	Faraday's constant
f_s (-)	spacer shadow factor
G (m^3 m^{-2} s^{-1})	generic volumetric water flux
GPD (W m^{-2})	gross power density
i (A m^{-2})	current density
I (A)	current intensity
J (mol m^{-2} s^{-1})	molar flux
l (m)	generic length
L (m)	spacer length
L_p (m^3 m^{-2} s^{-1} Pa^{-1})	water permeability
L_x (m)	average distance between the inlet and the outlet spacer holes
m (mol kg^{-1})	solution molality
M (g mol^{-1})	molar mass
n_h (-)	number of water molecules dragged by the solvation shell
N (-)	number of cell pairs
N_{holes} (-)	number of inlet (outlet) spacer holes
Q (m^3 s^{-1})	volume flow rate
r (Ω m^2)	generic areal electrical resistance
r_A (-)	first constant in the correlations for IEM electrical resistance
r_B (-)	second constant in the correlations for IEM electrical resistance
r_C (-)	third constant in the correlations for IEM electrical resistance
r_D (-)	fourth constant in the correlations for IEM electrical resistance
R (Ω)	generic electrical resistance
R_g (J mol^{-1} K^{-1})	gas constant

Sh (-)	Sherwood number
t (-)	generic ion transport number
T (K)	temperature
U (V)	potential difference over the series of resistors R_u and R_{bl}
U_{ext} (V)	potential difference over the external load
V (V)	generic voltage
x (m)	coordinate along the flow direction

Greek letters

α (-)	permselectivity
α_A (-)	first constant in the correlations for IEMs permeselectivities
α_B (-)	second constant in the correlations for IEMs permeselectivities
α_C (-)	third constant in the correlations for IEMs permeselectivities
γ (-)	activity coefficient
Λ (mS l mol^{-1})	equivalent conductivity
π_{osm} (Pa)	osmotic pressure
ρ (kg m^{-3})	mass density
σ (S m^{-1})	solution conductivity
ϕ (-)	osmotic coefficient
ψ_p (-)	loss of GPD due to shunt currents

Subscripts

av	average over the channel length
AEM	anion-exchange membrane
bl	blank resistance
c	concentrate solution
CEM	cation-exchange membrane
$cond$	conductive flux
$count$	counter-ion
d	diluate solution
$diff$	diffusive flux
$down$	lower branch
$e.\ osm$	electro-osmotic flux
ext	external electrical circuit
IEM	ion-exchange membrane
int	solution-side membrane interface
j	index for the generic current ingoing to or outgoing from a node
k	index for the cell position [1;N]
man	generic manifold (*collector* or *distributor*)
$no\ par$	no presence of parasitic currents
oma	out of the active membrane area
osm	osmotic flux
sol	generic solution compartment (either diluate, *d*, or concentrate, *c*)
tot	total flux of salt
u	external load
up	upper branch
w	water
x	generic longitudinal branch (*up* or *down*)
0	infinite dilution condition

as an optimization criterion, given the high cost of the membranes [19–22].

Several detrimental phenomena affect the performance of ED/RED processes. The most investigated are (i) co-ion transport and (ii) water transport through the membranes, (iii) uphill transport and effects of divalent ions on membrane resistance and permselectivity, (iv) concentration polarization, and (v) energy spent for pumping the solutions.

The first three depend on membrane properties, such as fixed charge density [23], water permeability [24,25] and monovalent-selectivity [26,27], as well as on solutions concentration and composition. The fourth and fifth phenomenon depend strongly on the fluid-dynamic conditions [7,10,28–30]. Other aspects concern the spacer shadow effect [7,31,32], and membrane deformation along with its effects [33–35].
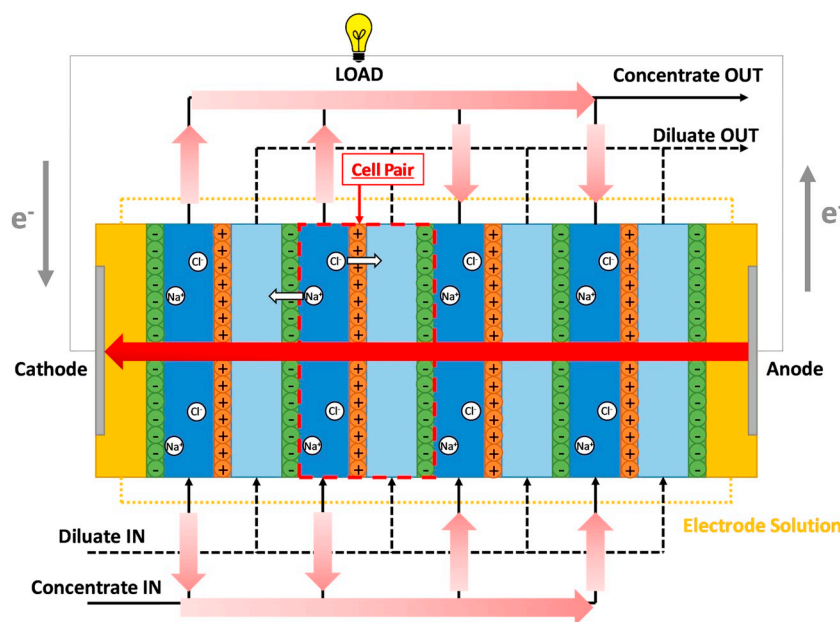
Fig. 1. Schematic drawing of a RED stack. The large red arrow from the anode to the cathode indicates the desired direction of the electric current; the other large pink arrows indicate the electrical parasitic pathways (shortcuts) via manifolds in the concentrate hydraulic circuit.

1.2. Literature review and aim of this work

Ionic shortcut currents (known also as shunt currents, leakage currents or parasitic currents via manifolds) are a parasitic phenomenon in ED/RED units. They originate since the repetitive units of an ED/RED module are arranged electrically in series but hydraulically in a parallel fashion. Therefore, channels of the same solution subjected to a voltage difference act as "salt bridges" offering alternative "parasitic" pathways (Fig. 1), especially in the low-resistance concentrate circuit. As a result, a partial transport of the ionic current occurs along the channels and through the manifolds, rather than across the IEMs in the direction perpendicular to them.

The effects of shortcut currents in RED/ED units can be explained with the help of the schematic drawings reported in Figs. 2 and 3, respectively. In RED, for any given external electric current, which is the useful one delivered to the external load, the occurrence of the shortcut currents in a parallel branch via manifolds leads to an increase of the electric current flowing through the stack in the direction perpendicular to the membranes (Fig. 2). This effect occurs also under open circuit conditions, i.e. a completely parasitic internal current flows within the stack with a null external current. From the increase of the internal current it follows that, for any external current, Ohmic and non-Ohmic (salinity gradient consumption and concentration polarization) voltage drops increase. Therefore, the stack voltage and the power delivered to the external load are lower.

Similar statements can be argued for ED. For any useful internal current, depending on the desired desalted/concentrated product, the shunt current in the parallel branch inside the stack requires a higher external current (lower current efficiency). Since the stack voltage is fixed by the desired generation of salinity gradient and the useful current, a higher power consumption is required.

Of course, much more complex circuits represent real stacks, including several channels and parasitic pathways, the transport of electric current by two ionic species and the presence of non-perfectly permselective membranes. Overall, the presence of shortcut currents has eventually detrimental effects on the performance of the process, reducing its efficiency.

There are several experimental evidences of shunt currents and their effects. In ED/RED, leakage currents lessen the apparent stack resistance [36]. The parasitic pathways may be thought ideally as parallel electric paths (Figs. 2a–3a), hence they reduce the equivalent stack resistance.
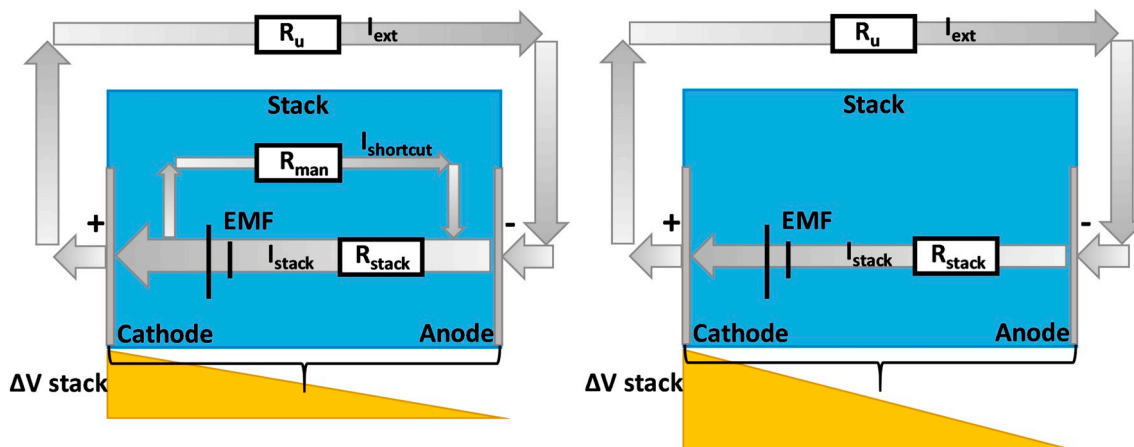

Fig. 2. Simplified diagrams of the electric currents flowing inside the stack in a RED process. a) with parasitic currents, b) without parasitic currents.

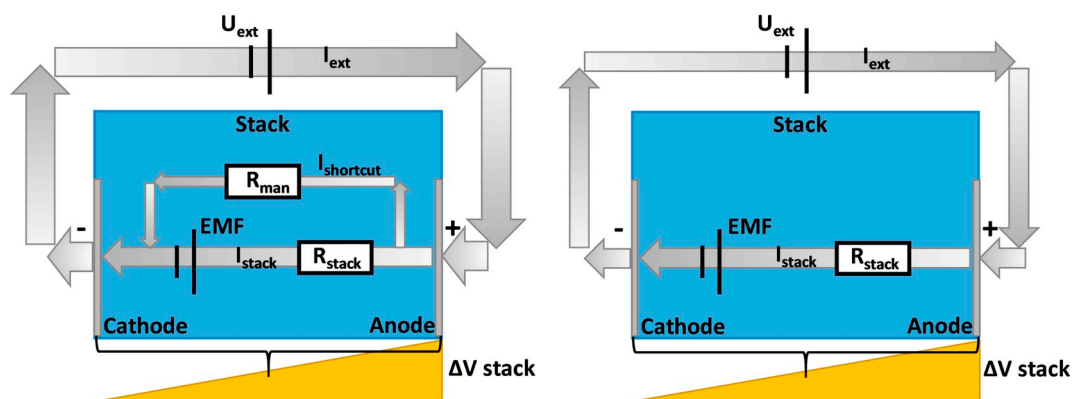**Fig. 3.** Simplified diagrams of the electric currents flowing inside the stack in an ED process. a) with parasitic currents, b) without parasitic currents.

In RED, the measured Open Circuit Voltage (OCV) is lower than the ideal one (without the parasitic current effect), i.e. it does not increase proportionally with the cell pairs number [65], because leakage currents cause the "self-discharge" of the salinity gradient, thus lowering the apparent average permselectivity [38]. This happens also under closed circuit [38], thus reducing the produced power [65]. Another possible electric bypass may be given by the connection of the electrode compartments using a reversible redox couple [39]. However, the tubing length is usually sufficient to give an electrical resistance so high as to make this shunt current negligible. Moreover, shortcut currents may cause an excessive overheating (ED), with consequent fall of the current efficiency [40], and even irreversible damage.

The amount of shunt currents depends on the relative importance of the electrical resistance of the bypasses. Whereas leakage currents are hardly detectable at low salt concentration [41], they lead to the variation of the stack potential distribution at higher salt concentrations [42]. The length of the ionic bypass and their cross sectional area play an important role likewise the conductivity of the electrolyte solutions [42]. In addition, the number of cell pairs is crucial. Particularly, the higher the number of repetitive units, the higher the effect of the shunt currents [65], due to the larger amount of parasitic pathways and to the larger voltage available.

The isolation of blocks of repetitive units may prevent the leak of currents through the manifolds [43]. The distribution of the solutions into the channels may be performed by rotative valves, hence reducing the parasitic pathways [44]. Moreover, the use of thin plastic film around the inlet/outlet holes of the membranes allows for the electrical insulation of the membrane active area close to the distributors and collectors, thus reducing shunt currents and their impact [40].

Typical ED/RED applications where stacks have low-resistance paths through the concentrate circuit and, thus, may be affected by significant shunt currents, are: ED of seawater, e.g. for salt production [36,42,43,45,46], ED metathesis [40], RED with seawater [39,65], or concentrated brines [12,15,16,22,38], including closed-loop systems [48,49], and ED/RED with bipolar membranes [50].

Despite their detrimental effects on the process efficiency, shunt currents have been explicitly modelled only in very few works. With reference to ED systems, Mandersloot and Hicks [36] gave a simplified equation of the fraction of the electrical leakage, highlighting the role of the ratio between the manifolds and the cell pair electric resistances. Similarly, Doležel and Keslerová [42] provided an expression of the leakage current putting the emphasis on the role of the ratio between the solutions and the membrane conductivities. Tanaka [45] developed a model following a purely Ohmic approach, based on the equivalent electric circuit formulated by Wilson [51].

Regarding RED systems, Rubinstein et al. [50] developed a mathematical model to simulate a simplified electric circuit scheme. In particular, the model predicted the "saturation" effect of the leakage currents on the OCV as the number of cell pairs increased in stacks with bipolar membranes.

A similar mathematical model was formulated by Veerman et al. [65], who included also the branch of the resistances of the electrode compartments and of the external load in the equivalent electric scheme. However, this model followed still a simplified approach, simulating the drain branches of the concentrate solution only. The model predictions showed that leakage currents lead to a reduction of the stack potential and to a loss of electric power over the external load, thereby decreasing the process efficiency. Simulation results were useful to describe the shortcut currents phenomena and to quantify their impact on the process performance. However, the model was not "fully predictive", being limited to the simulation of systems experimentally tested for the calibration.

In the work of Tedesco et al. [12], the shortcut currents were modelled within a comprehensive multi-scale process simulator with higher predictive capabilities, where salt and water fluxes, along with mass balances, were simulated at the cell pair scale, while the electrical behaviour of the stack was simulated by an equivalent circuit of the entire unit. The two levels of modelling interact each other, providing a powerful simulation tool, which does not require any calibration, but only easily measurable membrane properties (electrical resistance, permselectivity, water and salt permeability). However, no experimental validation of the parasitic currents model was provided, and any discussion about the specific influence of the leakage currents on the performance of RED stacks was reported.

Despite several multi-scale semi-empirical models have demonstrated their effectiveness in the simulation of both the ED [52,53] and RED [7,48,55] processes, they often do not include at all the shunt currents, by assuming an identical behaviour of all cell pairs. Therefore, the simulation results (i) are affected by some approximation when they are used to predict the operation of industrial-size units with hundreds of cell pairs fed by highly concentrated solutions, (ii) or refer to special stacks suitably tailored to minimize the shunt currents.

The aim of this work is to put light on the parasitic currents phenomena in RED applications, through the development of a mathematical model experimentally validated. In particular, a semi-empirical simulator with distributed parameters was developed following a multiscale approach. This model requires only input parameters concerning the membrane properties, which are easily accessible by experiments, thus overcoming the typical limits of calibrated Ohmic models, and allowing for the prediction of the operation and performance of RED units with different design features and operating conditions. Once validated under several experimental conditions, the simulation results were discussed with particular focus on the distribution of parasitic currents and on their influence on the RED process performance. A

sensitivity analysis highlighted critical conditions where shunt currents play a crucial role was performed, thus providing important suggestions for the design of improved industrial stacks with higher efficiency.

2. Multi-scale model

The modelling strategy follows a multi-scale approach, which includes two different levels of simulation: the cell pair, and the stack. The cell pair is simulated by a 1-D model that computes salt and water fluxes, mass balances (differential equations), electromotive force and cell resistance along the flow direction. The stack model contains only algebraic equations for the simulation of the equivalent electrical circuit, thus predicting (i) the distribution of the electric current throughout the stack, including the external circuit, and (ii) the performance of the RED process. The integrated multi-scale model was implemented in the gPROMS® Model Builder platform [56].

2.1. Cell pair model

The 1-D cell pair model simulates all the main transport mechanisms between the concentrate and diluate channel through the membranes of each cell. The Ohmic, diffusive, osmotic and electro-osmotic fluxes are calculated, along with water and salt mass balances. Moreover, the electric resistance of the cell pair is computed. All variables are distributed along the main flow direction x. The use of 100 intervals was found sufficient to obtain results unaffected by the discretization degree. Note that the cell pair model resolves distinctly (i.e. one by one) all the cell pairs of the stack, as the distribution of the electric current computed by the stack model causes that the cell pairs behave in a different way each other. Therefore, the equations of the cell pair model refer to the k-th cell, with k varying from 1 to the total number of cell pairs N.

Concentrate and diluate consist of NaCl aqueous solutions, whose physical properties (i.e. mass density, viscosity and electrical conductivity) are calculated by the correlations reported in Appendix A. The activity and osmotic coefficients are provided by the Pitzer virial equations reported in the literature [57,58].

Following the Nernst-Planck approach, the total salt flux $J_{tot,\ k}$ through the membranes is the sum of the conductive and diffusive fluxes:

$$J_{tot,k}(x) = J_{cond,k}(x) + J_{diff,k}(x) \tag{1}$$

The conductive flux $J_{cond,\ k}$ can be calculated as

$$J_{cond,k}(x) = \frac{i_k(x)[t_{count,CEM,k}(x) - (1 - t_{count,AEM,k}(x))]}{F} \tag{2}$$

where i_k is the cell current density, $t_{count,\ CEM,\ k}$ and $t_{count,\ AEM,\ k}$ are the sodium and chloride ions transport numbers in the CEM and AEM, respectively (i.e. transport numbers of the counter-ions), and F is the Faraday constant. The transport numbers are evaluated from the permselectivity, as reported in Appendix A.

The diffusive flux is provided by the formula

$$J_{diff,k}(x) = \frac{2\,D_{IEM}}{d_{IEM}}(C_{c,k}(x) - C_{d,k}(x)) \tag{3}$$

in which D_{IEM} is the salt diffusive permeability across the membranes (see Appendix A), d_{IEM} is the membrane thickness, $C_{c,\ k}$ and $C_{d,\ k}$ are the concentrate and diluate salt concentrations, respectively.

The total water flux from the concentrate to the two adjacent diluate compartments $G_{w,\ k}$ (in $m^3\ m^{-2}\ s^{-1}$) is given by

$$G_{w,k}(x) = G_{osm,k}(x) + G_{e.osm,k}(x) \tag{4}$$

where $G_{osm,\ k}$ is the osmotic flux and $G_{e.\ osm,\ k}$ is the electro-osmotic flux.

The osmotic flux is given by

$$G_{osm,k}(x) = -2 L_p (\pi_{osm,c,k}(x) - \pi_{osm,d,k}(x)) \tag{5}$$

in which L_p is the water permeability in the membranes, which is a constant equal to $2.22 \cdot 10^{-14}\ m^3\ m^{-2}\ s^{-1}\ Pa^{-1}$ and $\pi_{osm,\ c,\ k}$ and $\pi_{osm,\ d,\ k}$ are the concentrate and diluate osmotic pressures, which are calculated as:

$$\pi_{osm,sol,k}(x) = 2\,R_g\,T\,\Phi_k(x)\,C_{sol,k}(x) \tag{6}$$

in which the coefficient equal to 2 is the value of the van 't Hoff factor for NaCl, R_g is the gas constant, T is the temperature of the system, Φ_k is the osmotic coefficient, calculated according to Pitzer's virial equations [57,58], and $C_{sol,\ k}$ is the salt concentration in the k-th channel (either concentrate or diluate).

The electro-osmotic flux $G_{e.\ osm,\ k}$ is calculated by the equation

$$G_{e.osm,k}(x) = n_h\,J_{tot,k}(x)\,\frac{M_w}{10^3\,\rho(x)} \tag{7}$$

where M_w is the water molar mass (in $g\ mol^{-1}$), ρ is the solution density, n_h is the so called hydration number and it is equal to the number of water molecules dragged by the solvation shell of the ions salt. This number is fixed to 7 because the hydration number of sodium ion is equal to 6 and that of chloride ion is 8 [59].

The salt concentration and the volume flow rates profiles along the channels length are derived from the differential mass balances. The following equation shows the salt mass balance

$$\frac{d(Q_{sol,k}(x)\,C_{sol,k}(x))}{dx} = \pm J_{tot,k}(x)\,b \tag{8}$$

where $Q_{sol,\ k}$ is the volumetric flow rate in the k-th channel (either concentrate or diluate), and b is the spacer width; the sign $\pm$ depends on the compartment, i.e. $+$ for the diluate, $-$ for the concentrate. By neglecting the variations of the solution density, the global mass balances can be expressed by the following equation:

$$\frac{dQ_{sol,k}(x)}{dx} = \pm G_{w,k}(x)\,b \tag{9}$$

For what concerns the electrical variables, the local electromotive force of the cell pair EMF_k is given by the sum of the contributions from the two membranes:

$$EMF_k(x) = EMF_{CEM,k}(x) + EMF_{AEM,k}(x) \tag{10}$$

The electromotive force of either membrane $EMF_{IEM.\ k}$ is computed taking into account concentration polarization effects as:

$$EMF_{IEM,k}(x) = \alpha_{IEM,k}(x)\frac{R_g\,T}{F}\ln\left(\frac{m_{c,int,IEM,k}(x)\,\gamma_{c,int,IEM,k}(x)}{m_{d,int,IEM,k}(x)\,\gamma_{d,int,IEM,k}(x)}\right) \tag{11}$$

where $\alpha_{IEM,\ k}$ is the membrane permselectivity, $m_{c,\ int,\ IEM,\ k}$ and $m_{d,\ int,\ IEM,\ k}$ are the salt molal concentrations in the concentrate and diluate, respectively, at the solution-membrane interface, and $\gamma_{c,\ int,\ IEM,\ k}$ and $\gamma_{d,\ int,\ IEM,\ k}$ are the concentrate and diluate solutions activities at the same locations, calculated using the Pitzer virial equations [57,58]. The four (two for AEM and two for CEM) solution-membrane interface molar concentrations are calculated taking into account the diffusive flux at the interface (neglecting the diffusive flux across the membrane) and the definition of the Sherwood number:

$$C_{d,int,IEM,k}(x) = C_{d,k}(x) + \frac{(t_{count,IEM,k}(x) - t_{count,d,k})\,i_k(x)\,2d_d}{F\,Sh_{d,IEM,k}(x)\,D_d\,C_d(x)} \tag{12}$$

$$C_{c,int,IEM,k}(x) = C_{c,k}(x) - \frac{(t_{count,IEM,k}(x) - t_{count,c,k})\,i_k(x)\,2d_c}{F\,Sh_{c,IEM,k}(x)\,D_c\,C_c(x)} \tag{13}$$

where $t_{count,\ d,\ k}$ and $t_{count,\ c,\ k}$ are the transport numbers of the counterion in the diluate and concentrate, d_d and d_c are the compartment (spacer) thicknesses for diluate and concentrate, $Sh_{d,\ IEM,\ k}$ and $Sh_{c,\ IEM,\ k}$ are the Sherwood numbers in the diluate and concentrate, and D_d and D_c are the salt diffusivities of concentrate and diluate solutions, respectively. Sherwood numbers are obtained from 3-D CFD simulations

[7,35,60]. The constant values used for the salt diffusivities are reported in Appendix A.

The local cell pair electrical resistance R_k is calculated by the sum

$$R_k(x) = R_{AEM,k}(x) + R_{CEM,k}(x) + R_{d,k}(x) + R_{c,k}(x) \quad (14)$$

with $R_{AEM,\ k}$ and $R_{CEM,\ k}$ being the anion- and cation- exchange membrane resistances, respectively and $R_{d,\ k}$ and $R_{c,\ k}$ being the diluate and concentrate channel resistances.

Membrane resistances are calculated as

$$R_{IEM,k}(x) = \frac{r_{IEM,k}(x)}{b\,\Delta x} \quad (15)$$

where $r_{IEM,\ k}$ is the areal membrane resistance empirically assessed (see Appendix A).

The electrical resistance of the generic compartment $R_{sol,\ k}$ (either concentrate, c, or diluate, d) is given by

$$R_{sol,k}(x) = f_s \frac{d_{sol}}{b\,\Delta x\,\sigma_{sol,k}(x)} \quad (16)$$

where f_s is the so-called spacer shadow factor, d_{sol} is the channel thickness (either concentrate, c, or diluate, d), Δx is the length of a discretization interval (i.e. equal to 1/100 of the channel length) and $\sigma_{sol,\ k}$ is the electrolyte solution conductivity calculated as a function of the salt concentration (see Appendix A). f_s is assumed to be equal to the inverse of the spacer-filled channel volume porosity (also called void ratio).

2.2. Stack model

The stack model simulates the electrical behaviour of the whole stack composed of any number of cell pairs, including the electrode compartments and the external circuit. It calculates the electric currents flowing in each branch and the voltage difference between the nodes of the equivalent electrical circuit shown in Fig. 4, thus allowing the prediction of the shunt currents and their impact on the stack performance.

Two longitudinal resistances are calculated for each channel, while a voltage source along with its relevant resistance are calculated per each cell pair. The other electrical resistances of the equivalent circuit include those in the manifolds (interposed between two channels of the same solution), in the electrode compartments and in the external load. A longitudinal current outgoing from the channel is assumed positive, while a longitudinal current ingoing into the channel is assumed negative. The cell current is positive if directed from right (anode, −) to

left (cathode, +). Electric currents through the manifolds, either distributor or collector, are assumed positive from left to right.

At each node of the electrical scheme, the Kirchhoff's node law is applied:

$$\sum_j I_j = 0 \quad (17)$$

in which I_j is the generic j-th electric current ingoing to or outgoing from each node of the equivalent electric circuit shown in Fig. 4 (see coloured circles), kept with the algebraic sign according to the convention just mentioned above.

The first Ohm law is applied over each resistance of the equivalent circuit. In particular, the voltage drop over each of the N-1 generic manifold resistances is computed as

$$\Delta V_{sol,man,k} = I_{sol,man,k} R_{sol,man,k} \quad (18)$$

where $\Delta V_{sol,\ man,\ k}$ is the k-th voltage difference between two consecutive red (for concentrate) or blue (for diluate) nodes shown in Fig. 4 for a generic manifold (i.e. distributor or collector) and $R_{sol,\ man,\ k}$ is the electrical resistance of the k-th manifold. For the generic solution (i.e. diluate or concentrate) $R_{sol,\ man,\ k}$ is calculated as

$$R_{sol,man,k} = \frac{l_{man}}{N_{holes}\,\pi\frac{d_{man}^2}{4}\,\sigma_{sol,man,k}} \quad (19)$$

where N_{holes} is the number of inlet/outlet spacer holes, d_{man} is the manifold diameter, $\sigma_{sol,\ man,\ k}$ is the electrical conductivity of the solution flowing in the k-th manifold (i.e. distributor or collector), and l_{man} is given by the sum of the thicknesses of the cell pair elements:

$$l_{man} = d_{CEM} + d_{AEM} + d_c + d_d \quad (20)$$

To calculate $\sigma_{sol,\ man,\ k}$ the salt concentration along the manifolds is necessary. It is calculated by mass balances in the manifolds:

$$C_{sol,man,k} = \frac{C_{sol,man,k-1}\,Q_{sol,man,k-1} + C_{sol,k}(x=L)\,Q_{sol,k}(x=L)}{Q_{sol,man,k}} \quad (21)$$

$$C_{sol,man,1} = C_{sol,1}(x=L) \quad (22)$$

$$Q_{sol,man,k} = Q_{sol,man,k-1} + Q_{sol,k}(x=L) \quad (23)$$

$$Q_{sol,man,1} = Q_{sol,1}(x=L) \quad (24)$$

Eqs. (21) and (23) are applied for k in the interval [2;N-1].

The voltage drop over each resistance along the flow direction in the channel is given by
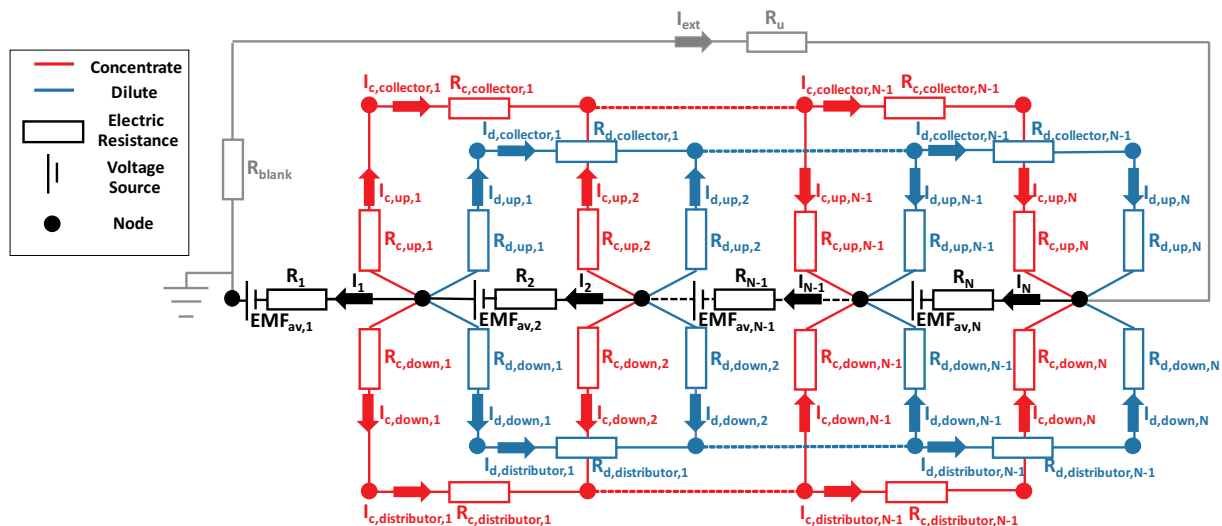

Fig. 4. Scheme of the equivalent electric circuit of the stack.

$$\Delta V_{sol,x,k} = I_{sol,x,k} \, R_{sol,x,k} \tag{25}$$

where $\Delta V_{sol,\,x,\,k}$ is the k-th voltage difference between two nodes, one red or blue and one black, consecutively placed for the generic solution (*sol*, i.e. diluate or concentrate) and for the generic longitudinal branch (*x* subscript, i.e. *up* or *down*), and $I_{sol,\,x,\,k}$ and $R_{sol,\,x,\,k}$ are the relevant electric current and resistance. Eq. (25) is applied for k in the range [1;N]. $R_{sol,\,x,\,k}$ ($R_{sol,\,up,\,k}$ and $R_{sol,\,down,\,k}$ in Fig. 4) are calculated as a series of a resistance in the membrane active area and a parallel of N_{holes}-resistances out of the membrane active area (Fig. 5). It is given by the relation:

$$R_{sol,x,k} = f_s \frac{L_x/2}{d_{sol} \, b \, \sigma_{sol,x,k}} + f_s \frac{l_{oma}}{\sigma_{sol,x,k} \, d_{sol} \, d_{oma} \, N_{holes}} \tag{26}$$

where f_s is the spacer shadow factor, L_x is the average distance between the inlet and the outlet spacer holes, l_{oma} and d_{oma} are the length and average width of the spacer region out of the active area (Fig. 5), $\sigma_{sol,\,x,\,k}$ is the conductivity of the solution calculated as a function of the average salt concentration between the middle of the channel and the outlet (for $x = up$) or the inlet (for $x = down$). Note that L_x simply coincides with the spacer length L in a rectangular spacer with inlet/outlet holes lying on lines parallel to L, as in Fig. 5. However, in general, they may differ each other, e.g. in spacers with a single inlet hole and a single outlet hole placed at the corners.

The (useful) electric current flowing in a cell pair (between two consecutive nodes along the black line in Fig. 4) in the direction perpendicular to the membranes is calculated as

$$I_k = \frac{(EMF_{av,k} - \Delta V_k)}{R_{av,k}} \tag{27}$$

in which $EMF_{av,\,k}$ is the average electromotive force given by

$$EMF_{av,k} = \frac{1}{L} \int_{x=0}^{x=L} EMF_k(x) dx \tag{28}$$

and $R_{av,\,k}$ is the average cell pair resistance given by

$$R_{av,k} = \frac{1}{L} \int_{x=0}^{x=L} R_k(x) dx \tag{29}$$

Eq. (27) is valid for k within the interval [1;N].

The electric current flowing through the external circuit (i.e. the grey branch in Fig. 4) I_{ext}, which is sent to the final user, is calculated as

$$I_{ext} = \frac{U}{R_u + R_{bl}} \tag{30}$$

in which U is the potential difference over the series of resistances R_u and R_{bl}. R_u is the external load resistance, while R_{bl} is the blank resistance, accounting for the resistance of electrode compartments and end-membrane, and for the overvoltage due to the electrochemical reactions at the electrodes.

The potential difference over the external load U_{ext} is computed as

$$U_{ext} = I_{ext} \, R_u \tag{31}$$

For what concern the performance parameters, the gross power density GPD (W m^{-2}) is calculated as

$$GPD = \frac{U_{ext} \, I_{ext}}{L \, b \, 2N} \tag{32}$$

Finally, in order to assess the impact of the shortcut currents, the relative loss of GPD with respect to an ideal case without parasitic currents was calculated:

$$\psi_p = \left(1 - \frac{GPD}{GPD_{no\,par}}\right) 100 \tag{33}$$

in which $GPD_{no\,par}$ is the gross power density calculated by simulations of the reference case neglecting parasitic currents, carried out by a simplified model where the stack is simply modelled without the shunt currents branches in the equivalent electric circuit (it reduces to a series of identical cell resistances and EMFs, together with the blank resistance and the external resistance). This kind of simulations and its outcomes are referred to as "ideal" in the following.

The simulations can be performed by letting the external resistance R_u to vary from open circuit condition ($R_u \to \infty$, thus finding the OCV) to short-circuit ($R_u \to 0$) in order to obtain the current-voltage curve, and thus the power curve. Results shown in the present paper usually refer to these two extreme conditions and to that where U_{ext} was fixed equal to OCV/2, which simulates the stack operation with the ideal (when no shunt currents) maximum power. Actually, the maximum power is obtained at lower values of the stack voltage, due to the ionic shortcut currents and to other reasons (e.g. the variation of the conditions along the channels). However, we found by both experiments and simulations that the discrepancy between the maximum power and the power delivered at OCV/2 was only of a few percent. Therefore, the OCV/2 condition was used to represent with very good approximation the maximum power condition.

3. Experimental

Experimental data useful for the model validation were collected using a lab-scale stack (provided by REDstack BV, The Netherlands) with a co-flow configuration. The cell pairs number ranged from 5 to 50. The stack was equipped with Fujifilm Type 10 membranes (Table 1, FujiFilm Manufacturing Europe B.V.), with an active area of 100 cm^2 (10 cm length, 10 cm width), along with 330 μm polyamide woven spacers (Deukum GmbH, Germany), made up of 4 inlet/outlet holes with a diameter of 6 mm each (see Fig. 5) with a volume porosity of 0.8. The membrane properties used as input for the model, evaluated by experimental tests as functions of the solutions concentrations, are
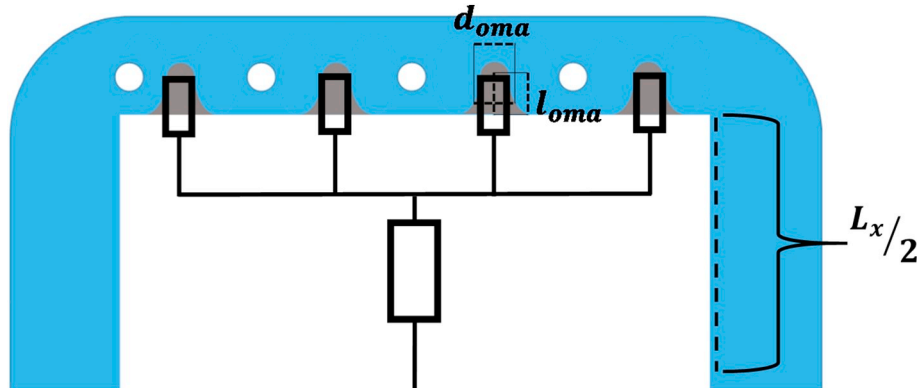

Fig. 5. Schematic representation of the electrical resistances along the longitudinal direction in the spacer-filled channel. Grey region is out of the membrane active area.

Table 1
Fujifilm type 10 membranes characteristics [61].

	CEM	AEM
Reinforcement	polyolefin	polyolefin
Thickness dry (μm)	125	135
Resistance (Ω cm^2)	1.7	2.0
Permselectivity (%)	95	99
Water permeation (ml bar^{-1} m^{-2} h^{-1})	6.5	6.5
Burst strength (kg cm^{-2})	2.8	2.8
pH stability ($-$)	1–13	1–13
Temperature stability (°C)	60	60

reported in Appendix A. The electrodes were of Dimensionally Stable Anodes (DSA)-type.

The NaCl concentration in the concentrate was fixed at 5 M (typical of concentrated brines), while that in the diluate was either 0.017 M or 0.05 M. A concentrated brine was used in the concentrate compartments in order to magnify the shortcut currents and their effects. The electrode rinse solution was a reversible redox couple with 0.1 M concentration of K$_3$Fe(CN)$_6$/K$_4$Fe(CN)$_6$ and 2.5 M concentration of NaCl as supporting electrolyte. From experiments with different number of cell pairs, the value of the areal blank resistance (electrode compartments with an additional CEM) was evaluated to be within the range ~60–72 Ω cm^2. The electrical conductivity of the solution was measured by a WTW 3310 conductometer.

Peristaltic pumps (Lead Fluid Technology *Co.*, Ltd.) were used to circulate all the streams, including the electrode rinse solution, through the RED stack. Concentrate and diluate were fed in once-through mode with a flow rate suitably chosen to guarantee a channel mean flow velocity of 1 cm s^{-1} in all tests. Conversely, the electrode solution was continuously recirculated to the reservoir. Current-voltage characteristics were recorded by using a 150 W DC Electronic Load (BK Precision 8540) operating in potentiostatic mode.

The experiments were performed at ambient temperature (~20 °C). All experiments were carried out four times and a fair reproducibility was found: average values along with relevant error bars are reported in the figures of Section 4.

4. Results and discussion

Modelling results and experimental data are reported and discussed in this section, which is divided in four sub-sections. First, the developed model is validated against a wide range of experimental results purposely collected with lab-scale stacks, by letting the design features

and the operating conditions to vary (Section 4.1). Second, the predictive capabilities of the model are shown and compared to a simple Ohmic simulation tool (Section 4.2). Third, the distribution of the electric current in the equivalent electrical circuit is analysed (Section 4.3). Finally, the influence of the manifolds diameter on the process performance is discussed with reference to large-scale stacks (Section 4.4).

4.1. Model validation

Fig. 6 shows the Open Circuit Voltage (OCV) (i.e. the voltage difference over the stack when no current flows in the external circuit) as a function of the cell pairs number, comparing experimental data and model predictions.

As it can be seen, both the experiments and the model predictions exhibit a deviation of the OCV from the ideal linear trend (no shunt currents) as the cell pairs number increases. A very good agreement between experiments and model was found at any concentration. Such deviation can be attributed to the effect of shunt currents. As a matter of fact, the higher the cell pairs number, the higher the number of the ion bypass pathways (see Fig. 4). This fact leads to the existence of a cell current even under open circuit condition, associated to an ion current through the manifolds (as they collect the ion current coming from the channels) and to a reduction of the OCV, as mentioned above. In other words, the occurrence of parasitic currents causes a higher consumption of the salinity gradient. Particularly, in the case of a higher concentration in the diluate (Fig. 6b), the lower driving force results in a lower OCV reduction compared to the 0.017 M case (Fig. 6a). Interestingly, the relative effect of parasitic current is lower, due to the lower resistance of the desired current path (perpendicular to the membranes). The maximum deviation at 50 cell pairs is 23.4% and 12.4% in the case of 0.017 M and 0.05 M, respectively (Fig. 6).

Data under closed circuit conditions are reported in Fig. 7, which shows the Gross Power Density (GPD) delivered by the stack when the applied voltage is equal to OCV/2 (very close to the ideal maximum GPD (i.e. without parasitic currents), as mentioned at the end of Section 2.2), as a function of the cell pairs number.

Overall, the model predictions are in good agreement with the experimental data. A variation is found at the lowest cell pairs number (where the effect of parasitic current is expected to be very low) for case a), probably due to an overestimation of the resistance in the electrode compartments (blank resistance). As a matter of fact, the error bars tend to reduce in stacks with a larger number of cell pairs (*N*), i.e. where the effect of the blank resistance is lower. This suggests that the lower
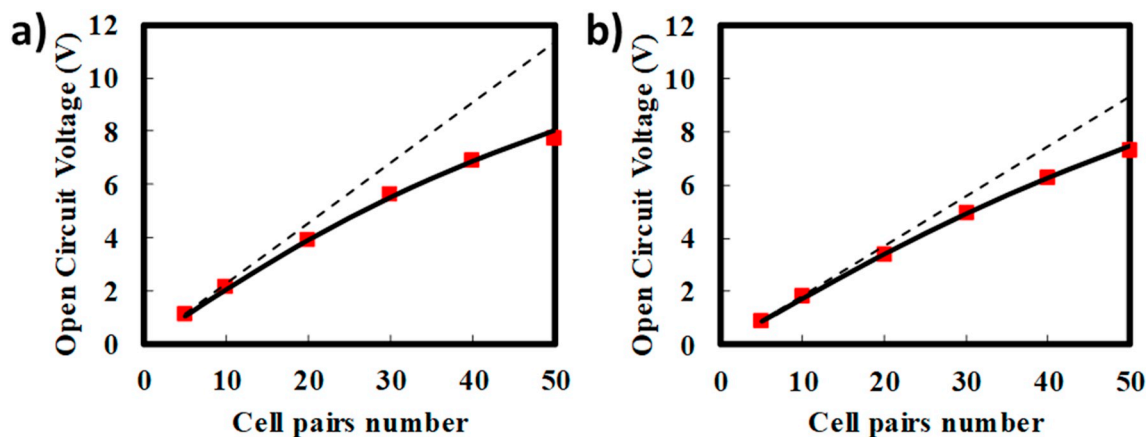

Fig. 6. Open Circuit Voltage (OCV) as a function of the cell pairs number in 10 × 10 cm^2 stacks with Fujifilm Type 10 membranes and with spacers provided with 4 inlet/outlet holes (diameter of 6 mm). Mean flow velocity of the electrolyte solutions in each channel equal to 1 cm s^{-1}. Symbols refer to experimental data, continuous lines to the model predictions, and broken lines to the ideal (i.e. no shunt currents) OCV. Inlet solution concentrations (NaCl): a) 0.017 M–5 M; b) 0.05 M–5 M. Areal blank resistance: a) 72 Ω cm^2, b) 60 Ω cm^2.

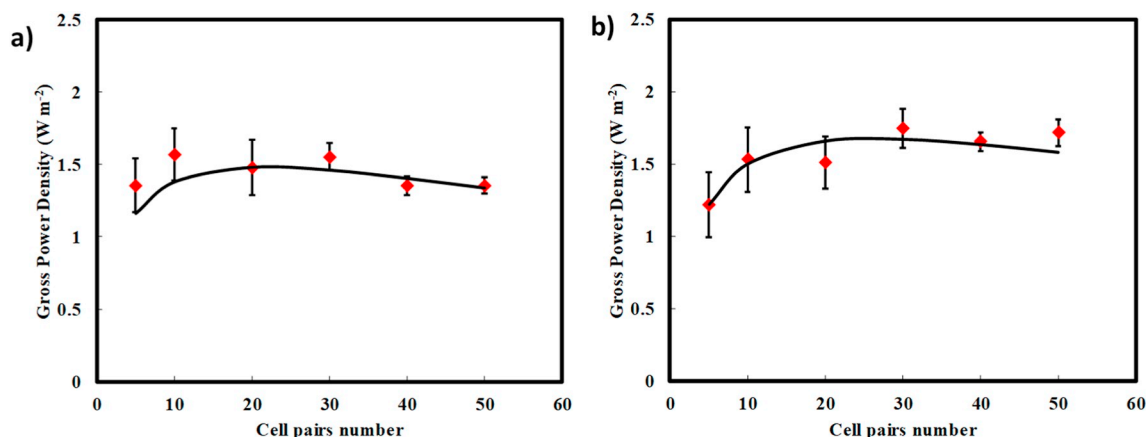**Fig. 7.** Gross Power Density (GPD) produced with an applied voltage equal to OCV/2 as a function of the cell pairs number in 10×10 cm^2 stacks with Fujifilm Type 10 membranes and with spacers provided with 4 inlet/outlet holes (diameter of 6 mm). Mean flow velocity of the electrolyte solutions in each channel equal to 1 cm s^{-1}. Symbols refer to experimental data, continuous lines to the model predictions. Inlet concentrations (NaCl): a) 0.017 M - 5 M; b) 0.05 M–5 M. Areal blank resistance: a) 72 Ω cm^2, b) 60 Ω cm^2.

reproducibility of the experimental results found at low values of *N* is likely caused by some variation in the electrode compartments or, more specifically, in the electrode rinse solution. For example, it can be altered by salt diffusion from the 5 M concentrated brine compartment.

An increase in GPD is observed as the number of cell pair increases, due to the decreasing relative impact of the blank resistance. This would lead to an asymptotic trend. Conversely, a maximum is exhibited by the GPD, because it is also affected by the parasitic currents, which count more at large N. The maximum occurs in stacks with ~21 and ~27 cell pairs fed by 0.017 M–5 M and 0.05 M–5 M solutions, respectively. Beyond the maximum point, the impact of the shortcut currents prevails, and the GPD decreases. The loss of power ψ_p (Eq. (33)) is ~20% and ~16% for the two feeding conditions, respectively, in stacks with 50 cell pairs, i.e. about one fifth and one sixth of the producible power density are lost due to shortcut currents.

Moreover, Table 2 shows the diluate and concentrate average (among the channels) conductivities at the outlet, by varying the external voltage difference in the stack with 50 cell pairs (largest effect of shunt currents) and for the case 0.017 M–5 M.

A fair agreement between experimental measurements and simulation results is found for the data reported in Table 2 (maximum discrepancy of 17%).

Parasitic currents and their effects on the process performance can be significant also in RED units fed by "standard" solutions of seawater and river water, depending on the constructive features of the stack. For example, non-negligible shunt currents may occur in stacks with high-resistance membranes. As a further validation step, results from the present model were also compared with data by Veerman et al. [65], which include both predictions of their own model and experimental results for stacks fed by artificial seawater and river water. In particular, Fig. 8a1 and Fig. 8b1 reports the OCV and Fig. 8a2 and Fig. 8b2 the Max Gross Power as functions of the cell pairs number for two stack configurations, respectively (different spacers and membranes, see figure caption).

The developed model provides outcomes which are in very good agreement with the data by Veerman et al. [65], thus obtaining a further validation. The ratio between the average manifold resistance of the concentrate solution, especially for a stack of 50 cell pairs (4.39 Ω for R1.0 stack and 1.17 Ω for F0.2 stack) and the average cell resistance (1.52 Ω for R1.0 stack and 0.246 Ω for F0.2 stack) plays a key role in the currents distribution within the stack. In particular, a higher average manifolds resistance (especially of the concentrate solution) and/or a lower average cell resistance lead to lower shunt currents and a consequent higher cell current (i.e. the useful one). In fact, within the

simulated conditions, the loss of power of decreased from ~22% for the R1.0 stack to ~6% for the F0.2 stack.

4.2. Model capabilities

As discussed in Section 1.2, the simplified model for parasitic currents by Veerman et al. [65] was based on the simulation of the stack electrical behaviour only. It is a "purely Ohmic" model calibrated on experimental data, which used constant electrical resistances and cell pair potentials. The obvious advantages of such a model were (i) ease of implementation and (ii) speed of computing. However, the predictive capability of Veerman et al. model is limited by the availability of experimental data for the calibration. The present multi-scale model, instead, following the approach by Tedesco et al. [12], is based on a process simulator assessing fluxes and mass balances at the cell pair scale fully coupled with the electrical behaviour of the stack. The higher complexity of this model and the larger computational effort that it requires for the simulations, are justified by the higher predictive capabilities.

This can be shown by a comparison between the two models in the simulation of generic conditions not tested experimentally. For comparison purposes, the simulations were performed also by implementing the model by Veerman et al. [65]. The input parameters used for the simulations performed with the Veerman model (in terms of electrical resistances and EMF) were calculated with the inlet conditions. Note that these simplifying assumptions, which are needed to follow the Veerman approach, affect the driving force, the channel resistances, and the resistances of the parasitic pathways. For example,

Table 2

Comparison between model outcomes and experimental results of the diluate and concentrate outlet conductivities for a 10×10 cm^2 stack with Fujifilm Type 10 membranes and with spacers provided with 4 inlet/outlet holes (diameter of 6 mm), equipped with 50 cell pairs, fed by 0.05 M–5 M inlet concentrations. Mean flow velocity of the electrolyte solutions in each channel equal to 1 cm s^{-1}. Areal blank resistance: 60 Ω cm^2.

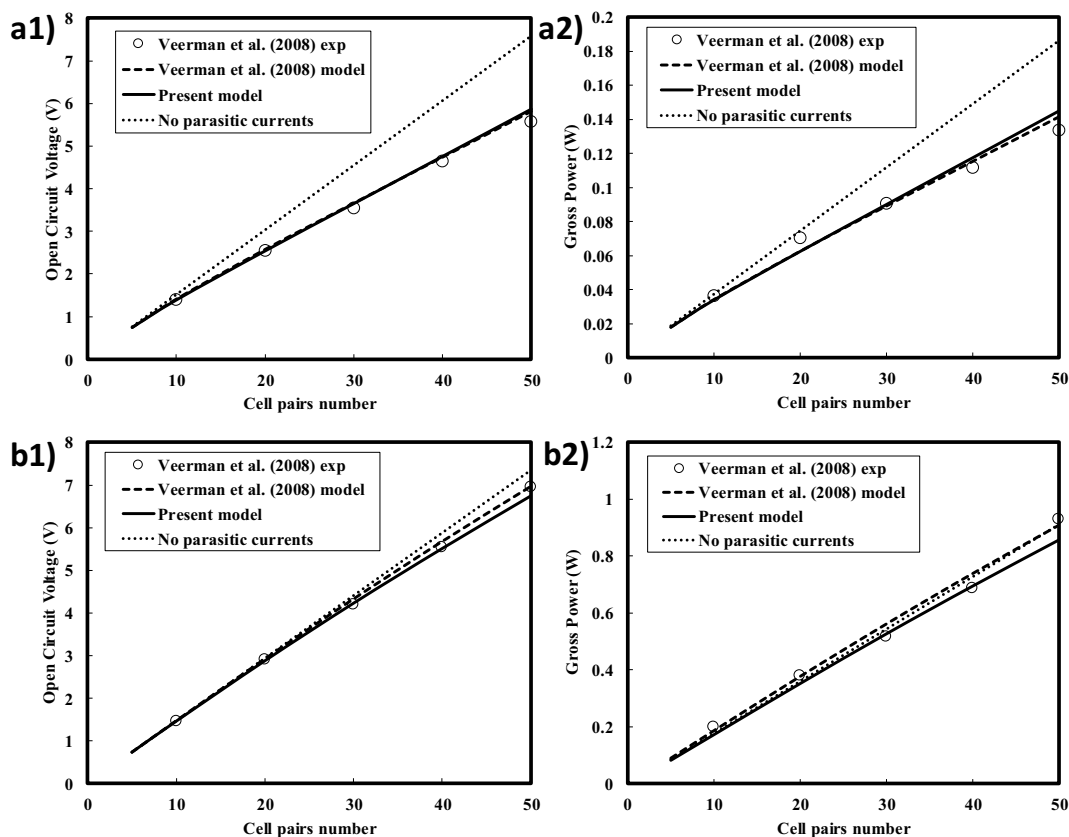| External voltage	Diluate outlet conductivity [mS cm^{-1}]		Concentrate outlet conductivity [mS cm^{-1}]	
	Experimental	Model	Experimental	Model
OCV	6.82	7.25	241	244
OCV/2	7.39	8.47	241	244
0 V	8.06	9.73	241	244

Fig. 8. Comparison between the present model predictions and data by Veerman et al. [65] as functions of the cell pairs number in stacks with 1 inlet/outlet hole (diameter of a1, a2) 10 mm and b1, b2) 8 mm). Dotted line refers to the ideal (i.e. no shunt currents). Mean flow velocity of the electrolyte solution in each channel equal to 1 cm s^{-1}. a1) Open Circuit Voltage and a2) Maximum Gross Power for stacks provided with Ralex membranes (0.65 mm thick) and spacers 1 mm thick [Stack named R1.0]; b1) Open Circuit Voltage and b2) Maximum Gross Power for stacks provided with Fumasep membranes (0.2 mm thick) and spacers 0.082 mm thick [Stack named F0.2]. Inlet concentrations (NaCl): 1 g l^{-1}–30 g l^{-1} (0.017 M–0.513 M). Areal blank resistance: a1, a2) 262 Ω cm^2, b1, b2) 12 Ω cm^2.

Fig. 9a1 and Fig 9a2 report the OCV and Fig. 9b1 and 9b2 the Gross Power Density as functions of the cell pairs number for stacks 10 cm long and 50 cm long, respectively.

There is a non-negligible discrepancy between the two models outcomes for short-channel stacks (10 cm length), especially in terms of OCV (Fig. 9a1). Note that the small discrepancy found in the GPD (Fig. 9a2) is only the complex result of the compensative effects of the Ohmic model assumptions. Therefore, larger differences can be found under other design and operating conditions. As a matter of fact, Fig. 9b1 and b2 show significant discrepancies between the two models in the simulation of stacks with long channels (50 cm), where the average conditions along the channels are very different from the inlet conditions. In particular, the simplifications (use of the inlet concentrations) needed in the model by Veerman et al. [65] led to an overestimation of the OCV and an underestimation of the GPD.

These results highlight the limits of an Ohmic model, and, at the same time, show that a multi-scale process simulator is a more effective, powerful and flexible tool for the simulation of RED units, including the effects of shortcut currents.

Finally, it can be drawn that stacks with shorter channels are affected at a larger extent from shortcut currents, due to the lower resistance of the parasitic pathways. In particular, under the conditions simulated in Fig. 9, a channel length of 50 cm leads to negligible shunt currents (Fig. 9b) in stacks with 5–50 cell pairs.

4.3. Prediction of electric current distributions

The developed model was used to investigate the distribution of the electric current in the lab-scale stack with 50 cell pairs used for the experiments (see Section 3). The maximum number of cell pairs used in the experiments was chosen in the present simulations in order to have the largest parasitic currents. Fig. 10 shows the distribution of the cell current (I_k) within the equivalent circuit of the stack (see Fig. 4) under different values of applied external voltage, i.e. OCV, OCV/2 (~maximum power) and 0 voltage (short-circuit).

The average cell current is 0.15 A, 0.41 A and 0.71 A and the external current (i.e. supplied to the external load) is 0 A, 0.33 A and 0.70 A in OCV, OCV/2 and 0 (short-circuit), respectively. The largest effects of the shortcut currents on the cell currents occur under open circuit conditions, as can be also observed from the higher curvature of the cell current profiles within the stack. This means that the relative weight of the current leakage with respect to the cell current is maximum under open circuit conditions and decreases as the external current increases, with significant variations. As a consequence, the departure of the cell current profile from the ideal flat trend (i.e. without the parasitic currents), which would occur in absence of shunt currents, is larger at higher values of the external voltage. The reason behind this behaviour can be explained as follows. Considering the simplified electrical circuit reported in Fig. 2a, one can easily derive that as the stack voltage increases, the cell current decreases, while the manifolds current increases. It should be noted that in the actual system simulated (Fig. 4) the electromotive forces and the resistances are not fixed, but depend on the stack voltage itself, which affects the solutions concentrations. However, despite these complications, simulation results showed that parasitic currents were higher as the stack voltage increases, both in absolute terms and in relative terms with respect to the cell currents. Note that the amount of shortcut currents and their effects on the process performance depend strongly on the electrical resistance of the
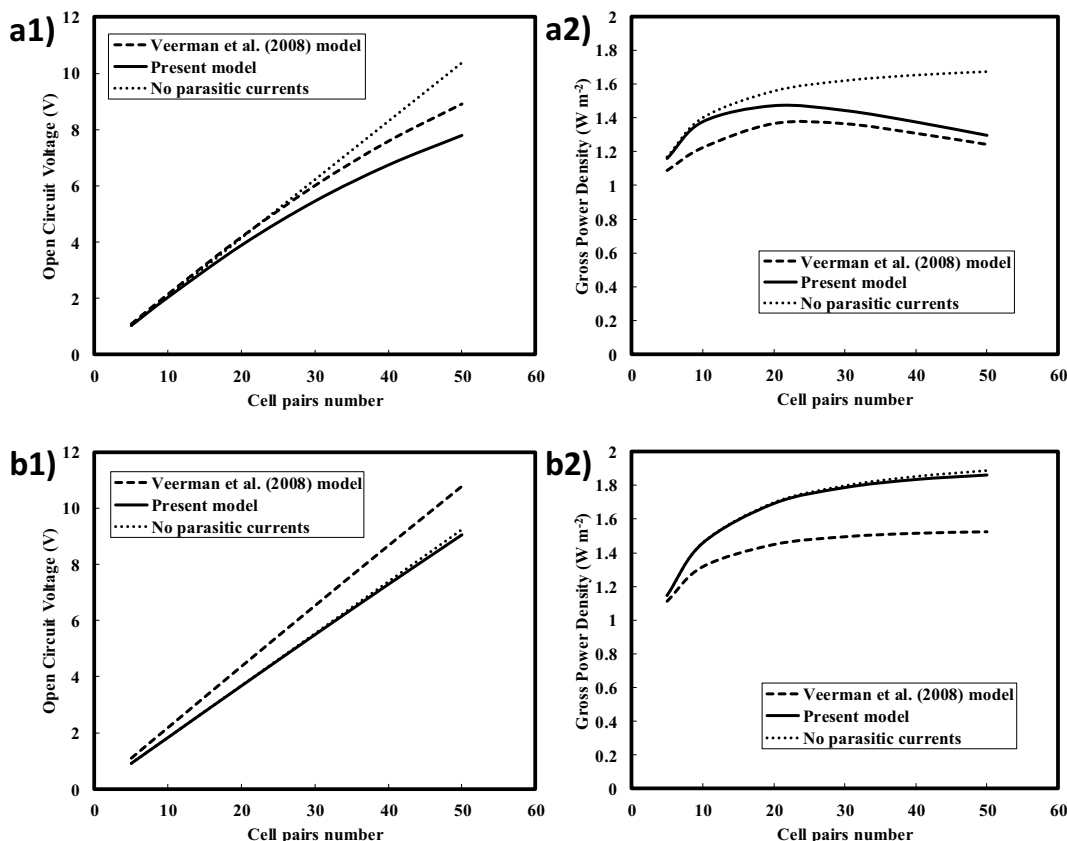
Fig. 9. Comparison between the predictions of the present model and those of the model by Veerman et al. [65] as functions of the cell pairs number. Dotted line refers to the ideal (i.e. no shunt currents). Mean flow velocity of the electrolyte solution in each channel equal to 1 cm s^{-1}. a1) Open Circuit Voltage and a2) Gross Power Density producible with an applied voltage equal to OCV/2 in 10 cm long and 50 cm wide stacks; b1) Open Circuit Voltage and b2) Gross Power Density producible with an applied voltage equal to OCV/2 in 50 × 50 cm^2 stacks. Spacers provided with 12 inlet/outlet holes (diameter of 1 cm). Fujifilm Type 10 membranes. Inlet solution concentrations (NaCl): 0.017 M - 5 M. Areal blank resistance: 72 Ω cm^2.
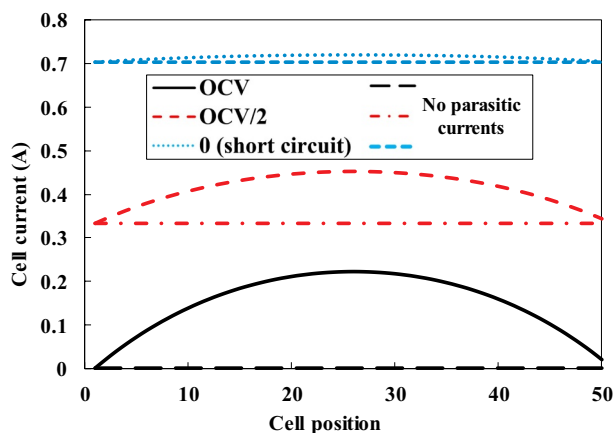
Fig. 10. Predicted profiles of cell current (I_k) at different values of the external voltage for 10 × 10 cm^2 stacks equipped with 50 cell pairs, with Fujifilm Type 10 membranes and with spacers provided with 4 inlet/outlet holes (diameter of 6 mm), fed by 0.017 M–5 M solutions. Mean flow velocity of the electrolyte solution in each channel equal to 1 cm s^{-1}. Areal blank resistance: 72 Ω cm^2.

manifolds and of the channels compared to the cell resistance, as discussed in the next sub-section.

Moreover, in Fig. 10 the highest percentage deviation of the cell current compared to the average is ~100%, ~20% and ~2%. Note that the small asymmetry in the equivalent circuit of Fig. 4 is reflected on the current distribution. For example, the cell current of the 1st cell pair differs from that of the last one (i.e. the 50th).

In order to explain the shape of the cell current profiles, Fig. 11 reports the distribution of the electric current along the lower longitudinal branches of the concentrate and the diluate channels $i_{c,\,down,\,k}$ and $i_{d,\,down,\,k}$ (see Fig. 4) for the same conditions of applied voltage considered in Fig. 10. The distribution in the upper branches is qualitatively and quantitatively identical and is not reported.

As shown in Fig. 11a, the maximum longitudinal leakage currents are ~0.01 A, ~0.005 A and ~0.0007 A in OCV, OCV/2 and 0 (short-circuit), respectively. They exhibit these largest values at the extreme channels, i.e. close to electrode compartments, while they vanish close to the central channels. A positive longitudinal current means that the electric current is outgoing the channel while a negative one is ingoing into the channel. With reference to the equivalent circuit reported in Fig. 4, this behaviour can be qualitatively intuited. Note that lower values of the longitudinal leakage currents are found as the stack voltage decreases (i.e. as the external current increases). Moreover, the driving force for the passage of the electric current along a channel branch is the voltage difference between the middle node of the channel and the distributor/collector node. Therefore, this voltage difference varies cell by cell and, in particular, it decreases towards the central part of the stack. The current profiles among the diluate channels (Fig. 11b) are qualitatively but non quantitatively the same of the concentrate channels. In particular, the current distribution in the diluate channels is two orders of magnitude lower than in the concentrate channels. As a matter of fact, the electric resistances of the diluate solution is high enough to make very low its contribution to diluate ducts shunt currents. On the other hand, a high electrical resistance in the diluate channel can make the cell pairs resistance higher than that in the concentrate manifolds, thus increasing the relevant parasitic currents.
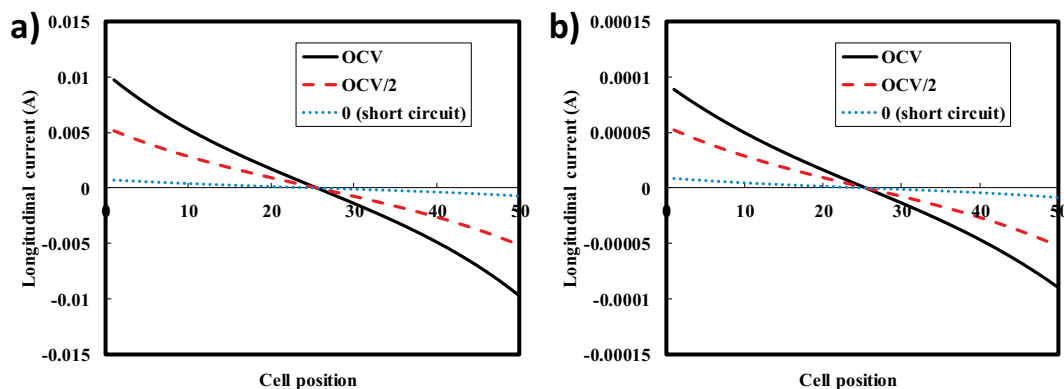
Fig. 11. Predicted profiles of the longitudinal current flowing along the lower branch of the a) concentrate channels $i_{c, down, k}$ and b) diluate channels $i_{d, down, k}$ at different values of the external voltage for 10×10 cm^2 stacks equipped with 50 cell pairs, with Fujifilm Type 10 membranes and with spacers provided with 4 inlet/outlet holes (diameter of 6 mm), fed by 0.017 M - 5 M solutions. Mean flow velocity of the electrolyte solution in each channel equal to 1 cm s^{-1}. Areal blank resistance: 72 Ω cm^2.

Longitudinal currents in the channels are collected/distributed in/by the manifolds. Electric current profiles along the lower concentrate and diluate manifolds (distributors), which are $I_{c, distributor, k}$ and $I_{d, distributor, k}$, respectively, are reported in Fig. 12.

The parasitic current via manifolds exhibits a trend qualitatively similar to the profile of the cell current (Fig. 10), with a maximum located approximately at the central part of the stack. As a difference, however, the average value of the parasitic current decreases as the external voltage decreases, while the opposite occurs for the average cell current (Fig. 10). This shows the lower relative weight of the shunt currents at lower values of the external voltage. The negligible amount of shunt currents along the diluate parasitic pathways is shown by the low values of the electric currents via the diluate manifolds (Fig. 12b).

4.4. Effect of the manifolds diameter in large-scale stacks

In order to assess the effects of parasitic currents in stacks with different manifolds size, a sensitivity analysis was performed by letting the manifolds diameter vary (from 2 mm to 14 mm). In this simulations set, the number of cell pairs was increased up to 500 and the active area to 50×50 cm^2, in order to mimic the features of a possible industrial scale stack. All the other constructive features, e.g. a inlet/outlet holes per each 4 cm (thus with a total of 12) and all the operating conditions were assumed equal to those of the experimental tests. Simulation results for the OCV are reported in Fig. 13.
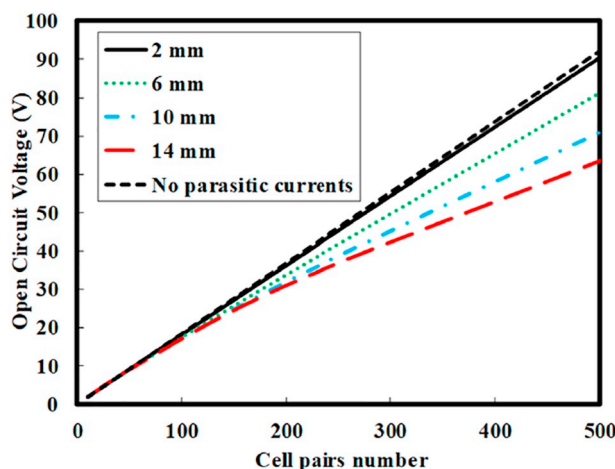

Fig. 13. Predicted Open Circuit Voltage (OCV) as a function of the cell pairs number in 50×50 cm^2 stacks with Fujifilm Type 10 membranes and with spacers provided with 12 inlet/outlet holes (diameter ranging from 2 mm to 14 mm). The dashed black line refers to the OCV predicted by the model neglecting the shunt currents. Inlet concentrations (NaCl): 0.017 M–5 M. Mean flow velocity of the electrolyte solution in each channel equal to 1 cm s^{-1}. Areal blank resistance: 72 Ω cm^2.
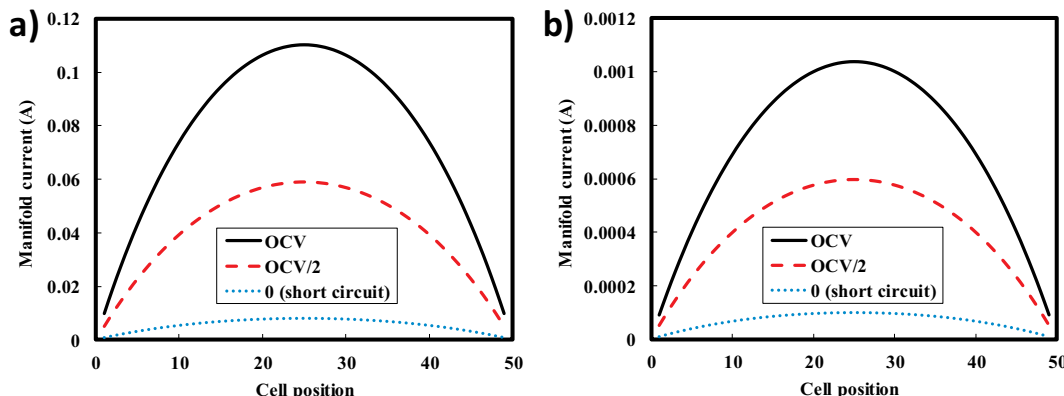

Fig. 12. Predicted profiles of current along the lower (distributor) a) concentrate manifolds $I_{c, distributor, k}$ and b) diluate manifolds $I_{d, distributor, k}$ at different values of the external voltage for 10×10 cm^2 stacks equipped with 50 cell pairs, with Fujifilm Type 10 membranes and with spacers provided with 4 inlet/outlet holes (diameter of 6 mm), fed by 0.017 M–5 M solutions. Mean flow velocity of the electrolyte solution in each channel equal to 1 cm s^{-1}. Areal blank resistance: 72 Ω cm^2.

As the inlet/outlet holes diameter increases, the OCV decreases significantly. Moreover, this effect is larger in stacks with a higher number of cell pairs. With 500 cell pairs, a manifolds diameter of 6 mm gave rise to a reduction in OCV of ~10% with respect the ideal case where parasitic currents are not simulated (simplified model, see Section 2.2); a manifolds diameter of 14 mm led to a loss of ~30%. By decreasing the manifolds diameter, it is possible to diminish strongly the shunt currents phenomena thanks to the higher electrical resistance of the parasitic pathways. In particular, shunt currents and their effects were almost negligible when the manifolds diameter was reduced at only 2 mm, with a maximum loss of OCV of 1.9% at 500 cell pairs with respect to the ideal case without shortcut currents.

The effects of the leakage currents are of higher practical interest in terms of delivered power under closed circuit conditions. Therefore, Fig. 14 reports the Gross Power Density and the corresponding loss ψ_p associated to parasitic currents when the applied voltage is equal to OCV/2.

As shown in Fig. 14a, leakage currents lead to the presence of a maximum in the Gross Power Density as a function of the cell pairs number. This occurs approximatively between 90 cell pairs and 60 cell pairs for stacks with 6 mm and 14 mm of manifolds diameter, respectively. The corresponding (i.e. at these maximum GPD) power loss due to parasitic currents is below 5%, as shown in Fig. 14b. By further increasing the cell pairs number, the increment of parasitic currents causes a reduction in GPD and a consequent larger loss of efficiency. The process performance depends significantly on the manifolds diameter, which affects the electrical resistance against the parasitic currents. The loss of power is between 8% and 25% in stacks with 500 cell pairs with 6 mm and 14 mm of manifolds diameter, respectively. A different behaviour characterizes stacks with very low manifolds diameter (2 mm), which exhibit an asymptotic behaviour in GPD up to the maximum cell pairs number considered here (i.e. 500) with a maximum loss of only ~1.3%.

More important, when standard seawater and river water were simulated, the maximum loss of GPD due to parasitic currents was of some % in the stacks considered here, due to the relatively high resistance of the parasitic pathways compared to the cell resistance in the direction perpendicular to the membranes.

5. Conclusion and future remarks

In this work, the parasitic phenomena of the shunt currents in RED units have been deeply investigated. A process model with distributed parameters was purposely developed, following a multi-scale simulation strategy. It integrates a 1-D cell pair level, computing salt and water fluxes, mass balances, electromotive force and cell resistance,

with an electrical equivalent circuit model for the whole stack. The model requires membrane properties which are available or easily accessible by experiments. Different stack designs and operating conditions can be simulated, including co- and counter-flow layouts. Model outcomes include the distribution of the variables along the flow direction in all the cells, along with the distribution of the electric current throughout the stack and in the external circuit. Therefore, the model is able to predict the process performance, including the electrical power delivered to the external load.

The model was validated under several design features and operating conditions via comparisons with both original experimental results collected with lab-scale stacks and data from the literature, showing good agreements. Compared to simple Ohmic models, the present process simulator exhibited higher predictive capabilities, being a more effective, powerful and flexible tool for the simulation of RED units, which includes shortcut currents effects.

A large number of simulations was performed by letting design features and operating conditions to vary in order to characterize widely the shortcut currents and to assess their impact in RED applications. The presence of parasitic pathways via manifolds led to a distribution of the cell current (electric current flowing perpendicularly to the membranes) and to an increase of its average value with respect to the external current (useful current delivered to the load). This resulted in an increase of the average cell voltage drop, thus reducing the power delivered to the external load.

The sensitivity analysis along with the experimental campaign highlighted that stacks with a large number of cell pairs, like those expected for industrial applications, may suffer from a significant drop in performance due to high shunt currents. The higher the number of repetitive units, the higher the number of the ion shortcuts and the larger the amount and impact of shunt currents. In particular, they play a crucial role when the electrical resistance of the parasitic pathways is relatively low compared to the cell pair resistance in the (desired) direction perpendicular to the membranes.

As the external voltage decreased (i.e. as the external current increased) the average cell current increased, while the average concentrate manifolds current decreased. Therefore, the current leakage and its relative weight with respect to the cell current were maximum under open circuit conditions and decreased at higher external currents. Moreover, parasitic currents were negligible in the diluate circuit.

Typical configurations presenting critical conditions for high shunt currents concern stacks fed by concentrated brines, or equipped with high resistance membranes, short channels or large manifolds. Simulation results, corroborated by experimental data, showed that lab-scale stacks (10 × 10 cm^2) fed with the conventional couple seawater - river water may be affected by large parasitic currents when high-
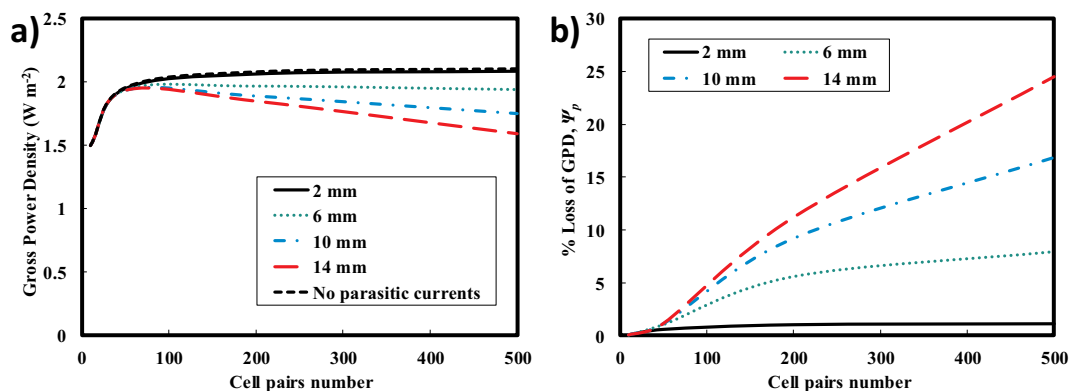

Fig. 14. Predicted a) Gross Power Density (GPD) producible with an applied voltage equal to OCV/2 and b) corresponding % loss due to parasitic currents (ψ_p) as functions of the cell pairs number in 50 × 50 cm^2 stacks with Fujifilm Type 10 membranes and with spacers provided with 4 inlet/outlet holes (diameter from 2 mm to 14 mm). The dashed line refers to the predictions of the model neglecting the shunt currents. Inlet concentrations (NaCl): 0.017 M–5 M. Mean flow velocity of the electrolyte solution in each channel equal to 1 cm s^{-1}. Areal blank resistance: 72 Ω cm^2.

resistance membranes are used. In particular, a loss of power density up to ~20% was found in a stack equipped with 50 cell pairs. In contrast, the use of stacks with low-resistance membranes can reduce significantly the shunt currents. However, such systems can experience intense shortcut currents in RED applications with concentrated brines (5 M), as shown by losses of power density of ~20% in units with 50 cell pairs.

In large-scale stacks, the huge amount of parasitic pathways given by hundreds of cell pairs is somehow compensated by the higher electrical resistance of the bypasses offered by longer channels. A sensitivity analysis was performed by letting the cell pair number and the manifolds diameter to vary, from 5 to 500 and from 2 mm to 14 mm, respectively, in 50×50 cm^2 stacks with low-resistance membranes. At OCV/2 conditions, although the shunt currents did not represent an important issue in the case of standard seawater – river water solutions, they affected the process performance when mixing the concentrated brine with river water, with a maximum loss of power density of ~25%.

The manifolds diameter is a crucial design parameter. However, smaller manifolds, which are less prone to shunt currents thanks to the higher resistance, could lead to issues of high pressure drops and poor flow distribution. Other measures can be implemented for the reduction of the shortcut currents, including the use of separated blocks of cell pairs with small parasitic circuits, but only cheap and constructively simple solutions can be attractive. In this direction, further studies are required for the development of efficient designs. For instance, a sub-model for the hydraulics of the channels (i.e. flow rate distribution along the cell pairs and relevant pressure drop calculation) would be beneficial for a reliable prediction of the net power density provided by the RED unit.

Finally, it is worth noting that the developed model can be adapted for the simulation of electrodialysis and other electromembrane processes, e.g. the same systems with bipolar membranes, with some suitable adjustments.

Appendix A. Correlations for the physical properties of electrolyte solutions and ion-exchange membranes

The mass density is computed following the correlation [62]:

$$\rho = 997 + 37.4 \frac{C}{1000} \tag{A.1}$$

in which ρ is the mass density expressed in kg m^{-3} and C is the NaCl concentration in solution in mol m^{-3}.

The electric conductivity is given by

$$\sigma = \frac{\Lambda C}{10000} \tag{A.2}$$

in which σ is the electrical conductivity in S m^{-1} and Λ is the equivalent conductivity mS l mol^{-1} cm^{-1}.

The equivalent conductivity Λ is evaluated using Jone and Dole's equation [63]:

$$\Lambda = \Lambda_0 - \frac{A_\Lambda \sqrt{\frac{C_k}{1000}}}{1 + B_\Lambda \sqrt{\frac{C_k}{1000}}} - C_\Lambda \frac{C}{1000} \tag{A.3}$$

where Λ_0 is the salt equivalent conductivity at infinite dilution and A_Λ, B_Λ and C_Λ are empirical parameters for NaCl.

The counter-ion transport numbers in membrane t_{IEM} are calculated by the equation:

$$t_{count,IEM} = \frac{1}{2} (\alpha_{IEM} + 1) \tag{A.4}$$

where α_{IEM} is the membrane permselectivity given by the relation:

$$\alpha_{IEM} = \alpha_{A,IEM} + \alpha_{B,IEM} \frac{C_c}{1000} + \alpha_{C,IEM} \frac{C_d}{1000} \tag{A.5}$$

where $\alpha_{A, IEM}$, $\alpha_{B, IEM}$ and $\alpha_{C, IEM}$ are constants found experimentally (Table A.1), C_c and C_d are the salt concentration in mol m^{-3} in the concentrate and diluate, respectively.

Table A.1
Constants in the correlation for the permselectivity of the Ion Exchange Membranes (Fujifilm type 10).

	CEM	AEM
$\alpha_{A,\,IEM}$	0.991	0.987
$\alpha_{B,\,IEM}$	-0.0441	-0.0441
$\alpha_{C,\,IEM}$	-0.2529	-0.18265

The areal membrane resistances (in Ohm m^2) are calculated by using the following empirical equations:

$$r_{IEM} = \left[r_{A,IEM} \left(\frac{C_c}{1000} \right)^2 + r_{B,IEM} \frac{C_c}{1000} + r_{C,IEM} + r_{D,IEM} \frac{C_d}{1000} \right] 10^{-4} \tag{A.6}$$

where $r_{A,\,IEM}$, $r_{B,\,IEM}$, $r_{C,\,IEM}$ and $r_{D,\,IEM}$ are constants whose values are listed in Table A.2.

Table A.2
Constants in the correlation for the electrical resistance of the Ion Exchange Membranes (Fujifilm type 10).

	CEM	AEM
$r_{A,\,IEM}$	0.4874	0.4874
$r_{B,\,IEM}$	-2.8119	-2.8119
$r_{C,\,IEM}$	7.218	7.21
$r_{D,\,IEM}$	-0.269	-0.141

The diffusive properties in the membranes and in the solutions are reported in Table A.3.

Table A.3
Salt diffusive permeability in the Ion Exchange Membranes and salt diffusivity in the solutions.

D_{IEM}	$4.52 \cdot 10^{-12}$ m^2 s^{-1}
D_c	$1.47 \cdot 10^{-9}$ m^2 s^{-1}
D_d	$1.57 \cdot 10^{-9}$ m^2 s^{-1}

References

[2] R.A. Tufa, S. Pawlowski, J. Veerman, K. Bouzek, E. Fontananova, G. di Profio, S. Velizarov, J. Goulão Crespo, K. Nijmeijer, E. Curcio, Progress and prospects in reverse electrodialysis for salinity gradient energy conversion and storage, Appl. Energy 225 (2018) 290–331, https://doi.org/10.1016/j.apenergy.2018.04.111.

[3] A. Cipollina, G. Micale, A. Tamburini, M. Tedesco, L. Gurreri, J. Veerman, S. Grasman, Reverse electrodialysis: applications, in: A. Cipollina, G. Micale (Eds.), Sustain. Energy from Salin. Gradients, 1st ed., Woodhead Publishing, Elsevier, Amsterdam, 2016, pp. 135–180 , https://doi.org/10.1016/B978-0-08-100312-1.00005-5.

[4] J. Veerman, D.A. Vermaas, Reverse electrodialysis: fundamentals, in: A. Cipollina, G. Micale (Eds.), Sustain. Energy from Salin. Gradients, 1st ed., Woodhead Publishing, Elsevier, Amsterdam, 2016, pp. 77–133, , https://doi.org/10.1016/B978-0-08-100312-1.00004-3.

[5] H. Strathmann, Ion-Exchange Membrane Separation Processes, First ed., Elsevier, Amsterdam, 2004, https://doi.org/10.1007/s13398-014-0173-7.2.

[6] O. Scialdone, C. Guarisco, S. Grispo, A.D. Angelo, A. Galia, Investigation of electrode material - redox couple systems for reverse electrodialysis processes. Part I: iron redox couples, J. Electroanal. Chem. 681 (2012) 66–75, https://doi.org/10.1016/j.jelechem.2012.05.017.

[7] M. La Cerva, M. Di Liberto, L. Gurreri, A. Tamburini, A. Cipollina, G. Micale, M. Ciofalo, Coupling CFD with a one-dimensional model to predict the performance of reverse electrodialysis stacks, J. Memb. Sci. 541 (2017) 595–610, https://doi.org/10.1016/j.memsci.2017.07.030.

[8] L. Gurreri, G. Battaglia, A. Tamburini, A. Cipollina, G. Micale, M. Ciofalo, Multi-physical modelling of reverse electrodialysis, Desalination 423 (2017) 52–64, https://doi.org/10.1016/j.desal.2017.09.006.

[9] R.E. Pattle, Production of electric power by mixing fresh and salt water in the hydroelectric pile [19], Nature 174 (1954) 660, https://doi.org/10.1038/174660a0.

[10] D.A. Vermaas, M. Saakes, K. Nijmeijer, Doubled power density from salinity gradients at reduced intermembrane distance, Environ. Sci. Technol. 45 (2011) 7089–7095, https://doi.org/10.1021/es2012758.

[11] H.K. Kim, M.S. Lee, S.Y. Lee, Y.W. Choi, N.J. Jeong, C.S. Kim, High power density of reverse electrodialysis with pore-filling ion exchange membranes and a high-open-area spacer, J. Mater. Chem. A 3 (2015) 16302–16306, https://doi.org/10.1039/c5ta03571f.

[12] M. Tedesco, A. Cipollina, A. Tamburini, I.D.L. Bogle, G. Micale, A simulation tool for analysis and design of reverse electrodialysis using concentrated brines, Chem. Eng. Res. Des. 93 (2015) 441–456, https://doi.org/10.1016/j.cherd.2014.05.009.

[13] R.A. Tufa, E. Rugiero, D. Chanda, J. Hnàt, W. van Baak, J. Veerman, E. Fontananova, G. Di Profio, E. Drioli, K. Bouzek, E. Curcio, Salinity gradient power-reverse electrodialysis and alkaline polymer electrolyte water electrolysis for hydrogen production, J. Memb. Sci. 514 (2016) 155–164, https://doi.org/10.1016/j.memsci.2016.04.067.

[14] R.S. Kingsbury, F. Liu, S. Zhu, C. Boggs, M.D. Armstrong, D.F. Call, O. Coronell, Impact of natural organic matter and inorganic solutes on energy recovery from five real salinity gradients using reverse electrodialysis, J. Memb. Sci. 541 (2017) 621–632, https://doi.org/10.1016/j.memsci.2017.07.038.

[15] F. Giacalone, M. Papapetrou, G. Kosmadakis, A. Tamburini, G. Micale, A. Cipollina, Application of reverse electrodialysis to site-specific types of saline solutions: a techno-economic assessment, Energy 181 (2019) 532–547, https://doi.org/10.1016/j.energy.2019.05.161.

[16] A. Tamburini, A. Cipollina, M. Tedesco, L. Gurreri, M. Ciofalo, G. Micale, The REAPower project: Power production from saline waters and concentrated brines, in: A. Basile, E. Curcio, I. Inamuddin (Eds.), Curr. Trends Futur. Dev. Membr, Elsevier, Amsterdam, 2019, pp. 407–448 , https://doi.org/10.1016/B978-0-12-813551-8.00017-6.

[17] M. Tedesco, A. Scalici, D. Vaccari, A. Cipollina, A. Tamburini, G. Micale, Performance of the first reverse electrodialysis pilot plant for power production from saline waters and concentrated brines, J. Memb. Sci. 500 (2016) 33–45, https://doi.org/10.1016/j.memsci.2015.10.057.

[18] A. Daniilidis, D.A. Vermaas, R. Herber, K. Nijmeijer, Experimentally obtainable energy from mixing river water, seawater or brines with reverse electrodialysis, Renew. Energy 64 (2014) 123–131, https://doi.org/10.1016/j.renene.2013.11.001.

[19] J. Veerman, M. Saakes, S.J. Metz, G.J. Harmsen, Reverse electrodialysis: a validated process model for design and optimization, Chem. Eng. J. 166 (2011) 256–268, https://doi.org/10.1016/j.cej.2010.10.071.

[20] R. Long, B. Li, Z. Liu, W. Liu, Reverse electrodialysis: modelling and performance analysis based on multi-objective optimization, Energy 151 (2018) 1–10, https://doi.org/10.1016/j.energy.2018.03.003.

[21] R. Long, B. Li, Z. Liu, W. Liu, Performance analysis of reverse electrodialysis stacks: channel geometry and flow rate optimization, Energy 158 (2018) 427–436, https://doi.org/10.1016/j.energy.2018.06.067.

[22] M. Ciofalo, M. La Cerva, M. Di Liberto, L. Gurreri, A. Cipollina, G. Micale, Optimization of net power density in reverse electrodialysis, Energy 181 (2019) 576–588, https://doi.org/10.1016/j.energy.2019.05.183.

[23] M. Tedesco, H.V.M. Hamelers, P.M. Biesheuvel, Nernst-Planck transport theory for (reverse) electrodialysis: I. effect of co-ion transport through the membranes, J. Memb. Sci. 510 (2016) 370–381, https://doi.org/10.1016/j.memsci.2016.03.012.

[24] M. Tedesco, H.V.M. Hamelers, P.M. Biesheuvel, Nernst-Planck transport theory for (reverse) electrodialysis: II. Effect of water transport through ion-exchange membranes, J. Memb. Sci. 531 (2017) 172–182, https://doi.org/10.1016/j.memsci.2017.02.031.

[25] M. Ciofalo, M. Di Liberto, L. Gurreri, M. La Cerva, L. Scelsi, G. Micale, Mass transfer in ducts with transpiring walls, Int. J. Heat Mass Transf. 132 (2019) 1074–1086, https://doi.org/10.1016/j.ijheatmasstransfer.2018.12.059.

[26] T. Rijnaarts, E. Huerta, W. Van Baak, K. Nijmeijer, Effect of divalent cations on RED performance and cation exchange membrane selection to enhance power densities, Environ. Sci. Technol. 51 (2017) 13028–13035, https://doi.org/10.1021/acs.est.7b03858.

[27] A.H. Avci, R.A. Tufa, E. Fontananova, E. Curcio, Reverse electrodialysis for energy production from natural river water and seawater, Energy 165 (2018) 512–521, https://doi.org/10.1016/j.energy.2018.09.111.

[28] D.A. Vermaas, E. Guler, M. Saakes, K. Nijmeijer, Theoretical power density from salinity gradients using reverse electrodialysis, Energy Procedia 20 (2012) 170–184, https://doi.org/10.1016/j.egypro.2012.03.018.

[29] L. Gurreri, A. Tamburini, A. Cipollina, G. Micale, M. Ciofalo, Pressure drop at low Reynolds numbers in woven-spacer-filled channels for membrane processes: CFD prediction and experimental validation, Desalin. Water Treat. 61 (2017) 170–182, https://doi.org/10.5004/dwt.2016.11279.

[30] S. Pawlowski, T. Rijnaarts, M. Saakes, K. Nijmeijer, J.G. Crespo, S. Velizarov, Improved fluid mixing and power density in reverse electrodialysis stacks with chevron-profiled membranes, J. Memb. Sci. 531 (2017) 111–121, https://doi.org/10.1016/j.memsci.2017.03.003.

[31] V.V. Wagholikar, H. Zhuang, Y. Jiao, N.E. Moe, H. Ramanan, L.M. Goh, J. Barber, K.S. Lee, H.P. Lee, J.Y.H. Fuh, Modeling cell pair resistance and spacer shadow factors in electro-separation processes, J. Memb. Sci. 543 (2017) 151–162, https://doi.org/10.1016/j.memsci.2017.08.054.

[32] S. Mehdizadeh, M. Yasukawa, T. Abo, Y. Kakihana, M. Higa, Effect of spacer geometry on membrane and solution compartment resistances in reverse electrodialysis, J. Memb. Sci. 572 (2019) 271–280, https://doi.org/10.1016/j.memsci.2018.09.051.

[33] G. Battaglia, L. Gurreri, G. Airò Farulla, A. Cipollina, A. Pirrotta, G. Micale, M. Ciofalo, Membrane deformation and its effects on flow and mass transfer in the electromembrane processes, Int. J. Mol. Sci. 20 (2019) 1840, https://doi.org/10.3390/ijms20081840.

[34] G. Battaglia, L. Gurreri, G. Airò Farulla, A. Cipollina, A. Pirrotta, G. Micale, M. Ciofalo, Pressure-induced deformation of pillar-type profiled membranes and its effects on flow and mass transfer, Computation 7 (2019) 32, https://doi.org/10.3390/computation7020032.

[35] G. Battaglia, L. Gurreri, A. Cipollina, A. Pirrotta, S. Velizarov, M. Ciofalo, G. Micale, Fluid–structure interaction and flow redistribution in membrane-bounded channels, Energies 12 (2019) 4259, https://doi.org/10.3390/en12224259.

[36] W.G.B. Mandersloot, R.E. Hicks, Leakage currents in electrodialytic desalting and brine production, Desalination 1 (1966) 178–193, https://doi.org/10.1016/S0011-9164(00)84017-5.

[38] A. Daniilidis, D.A. Vermaas, R. Herber, K. Nijmeijer, Experimentally obtainable energy from mixing river water, seawater or brines with reverse electrodialysis, Renew. Energy 64 (2014) 123–131, https://doi.org/10.1016/j.renene.2013.11.001.

[39] I. Choi, J.Y. Han, S.J. Yoo, D. Henkensmeier, J.Y. Kim, S.Y. Lee, J. Han, S.W. Nam, H.J. Kim, J.H. Jang, Experimental investigation of operating parameters in power generation by lab-scale reverse electro-dialysis (RED), Bull. Kor. Chem. Soc. 37 (2016) 1010–1019, https://doi.org/10.1002/bkcs.10810.

[40] N. Václavíková, L. Zich, M. Doležel, Pilot module for electrodialysis-metathesis protected against shunt currents, Desalin. Water Treat. 75 (2017) 320–324, https://doi.org/10.5004/dwt.2017.20446.

[41] R. Kodým, P. Pánek, D. Šnita, D. Tvrzník, K. Bouzek, Macrohomogeneous approach to a two-dimensional mathematical model of an industrial-scale electrodialysis unit, J. Appl. Electrochem. 42 (2012) 645–666, https://doi.org/10.1007/s10800-012-0457-6.

[42] M. Doležela, K. Keslerová, Measurement of non-effective electric current in electrodialysis stacks, J. Electrochem. Soc. 164 (2017) E276–E282, https://doi.org/10.1149/2.1481709jes.

[43] R. Yamane, M. Ichikawa, Y. Mizutani, Y. Onoue, Concentrated brine production from sea water by electrodialysis using ion exchange membranes, Ind. Eng. Chem. Process. Des. Dev. 8 (1969) 159–165, https://doi.org/10.1021/i260030a003.

[44] B.R. Bligh, Reverse Electrodialysis, Patent GB2197116A, (1988).

[45] Y. Tanaka, Ion Exchange Membranes - Fundamentals and Applications, Elsevier, Amsterdam, 2007, https://doi.org/10.1016/S0927-5193(07)12022-2.

[46] M. Sadrzadeh, T. Mohammadi, Treatment of sea water using electrodialysis: current efficiency evaluation, Desalination 249 (2009) 279–285, https://doi.org/10.1016/j.desal.2008.10.029.

[48] A. Tamburini, M. Tedesco, A. Cipollina, G. Micale, M. Ciofalo, M. Papapetrou, W. Van Baak, A. Piacentino, Reverse electrodialysis heat engine for sustainable power production, Appl. Energy 206 (2017) 1334–1353, https://doi.org/10.1016/j.apenergy.2017.10.008.

[49] F. Giacalone, P. Catrini, A. Tamburini, A. Cipollina, A. Piacentino, G. Micale, Exergy analysis of reverse electrodialysis, Energy Convers. Manag. 164 (2018) 588–602, https://doi.org/10.1016/j.enconman.2018.03.014.

[50] I. Rubinstein, J. Pretz, E. Staude, Open circuit voltage in a reverse electrodialysis cell, Phys. Chem. Chem. Phys. 3 (2001) 1666–1667, https://doi.org/10.1039/b010030g.

[51] J.R. Wilson, Demineralization by electrodialysis, Butterworths Sci. Publ. London. (1960), https://doi.org/10.1002/bbpc.19600641022.

[52] A. Campione, A. Cipollina, I.D.L. Bogle, L. Gurreri, A. Tamburini, M. Tedesco, G. Micale, A hierarchical model for novel schemes of electrodialysis desalination, Desalination 465 (2019) 79–93, https://doi.org/10.1016/j.desal.2019.04.020.

[53] N.C. Wright, S.R. Shah, S.E. Amrose, A.G. Winter, A robust model of brackish water electrodialysis desalination with experimental comparison at different size scales, Desalination 443 (2018) 27–43, https://doi.org/10.1016/j.desal.2018.04.018.

[55] E. Brauns, Salinity gradient power by reverse electrodialysis: effect of model parameters on electrical power output, Desalination 237 (2009) 378–391, https://doi.org/10.1016/j.desal.2008.10.003.

[56] Process Systems Enterprise, gPROMS, www.psenterprise.com/gproms 1997-2020.

[57] K.S. Pitzer, Thermodynamics of electrolytes. I. Theoretical basis and general equations, J. Phys. Chem. (1973), https://doi.org/10.1021/j100621a026.

[58] K.S. Pitzer, G. Mayorga, Thermodynamics of electrolytes. II. Activity and osmotic coefficients for strong electrolytes with one or both ions univalent, J. Phys. Chem. 77 (1973) 2300–2308, https://doi.org/10.1021/j100638a009.

[59] L. Han, S. Galier, H. Roux-de Balmann, Ion hydration number and electro-osmosis during electrodialysis of mixed salt solution, Desalination 373 (2015) 38–46, https://doi.org/10.1016/j.desal.2015.06.023.

[60] L. Gurreri, A. Tamburini, A. Cipollina, G. Micale, M. Ciofalo, Flow and mass transfer in spacer-filled channels for reverse electrodialysis: a CFD parametrical study, J. Memb. Sci. 497 (2016) 300–317, https://doi.org/10.1016/j.memsci.2015.09.006.

[61] Brochure of Fujifilm Membrane Technology, Ion Exchange Membranes for Water Purification, Version 1.0, 2018, 6 (2018) https://fujifilmmembranes.com/images/IEM_brochure_1_1_-final_small_size.pdf.

[62] T. Isono, Measurements of density, viscosity, and electrolytic conductivity of concentrated aqueous electrolyte solutions - 1. LiCl, NaCl, KCl, RbCl, CsCl, MgSO$_4$, ZnSO$_4$ and NiSO$_4$, Rika Gaku Kenkyujo Hokoku 56 (1980) 103–114.

[63] G. Jones, M. Dole, The electrical conductance of aqueous solutions of barium chloride as a function of the concentration, J. Am. Chem. Soc. 52 (1930) 2245–2256, https://doi.org/10.1021/ja01369a009.

[64] N.Y. Yip, D. Brogioli, H.V.M. Hamelers, K. Nijmeijer, Salinity gradients for sustainable energy: primer, progress, and prospects, Environ. Sci. Technol. 50 (2016) 12072–12094, https://doi.org/10.1021/acs.est.6b03448.

[65] J. Veerman, J.W. Post, M. Saakes, S.J. Metz, G.J. Harmsen, Reducing power losses caused by ionic shortcut currents in reverse electrodialysis stacks by a validated model, J. Membr. Sci. 310 (2008) 418–430, https://doi.org/10.1016/j.memsci.2007.11.032.